



Efficient sacrificial-agent-free solar H_2O_2 production over all-inorganic S-scheme composites

Miaoli Gu ^a, Yi Yang ^a, Liuyang Zhang ^{b,*}, Bicheng Zhu ^b, Guijie Liang ^c, Jiaguo Yu ^b

^a State Key Laboratory of Advanced Technology for Materials Synthesis and Processing, Wuhan University of Technology, Wuhan 430070, PR China

^b Laboratory of Solar Fuel, Faculty of Materials Science and Chemistry, China University of Geosciences, Wuhan 430074, PR China

^c Hubei Key Laboratory of Low Dimensional Optoelectronic Materials and Devices, Hubei University of Arts and Science, Xiangyang, Hubei 441053, PR China



ARTICLE INFO

Keywords:

Hydrogen peroxide
Pure water
Reactive oxygen species
Inorganic composite
Mechanism

ABSTRACT

Solar H_2O_2 generated from O_2 and H_2O is an economical and green protocol. However, most photocatalysts only perform well in the presence of sacrificial donors or the photocatalysts are composed by organic materials, thus hindering their applicability. Herein, an inorganic matrix, i.e. $ZnIn_2S_4@BiVO_4$ (ZIS@BVO), is constructed as a model catalyst for photocatalytic H_2O_2 production in non-sacrificial systems. Excellent performance ($1.8 \text{ mmol g}^{-1} \text{ h}^{-1}$) under visible-light is realized, and an apparent quantum yield of 5.18% is realized at 420 nm. Thorough investigation helps us to rationalize its exceptional performance and structural characteristics. Of note, the electron spin resonance spectroscopy results, in combination with scavenger capture experiments, reveal the discovery of an overlooked pathway. Specifically, except for the well-known two-electron oxygen reduction reaction (ORR), the involvement of 1O_2 intermediate is verified during the H_2O_2 generation. Beyond presenting high performance of the inorganic composites, this finding also discloses a different reaction path for H_2O_2 production.

1. Introduction

The increasing demand for sustainable and clean energy propels research on alternatives to fossil fuels with carbon-free energy sources. Hydrogen peroxide (H_2O_2) is not only a potential pollutant-free energy carrier, but also a high-value-added chemical that has been widely used in the chemical industry, electronics, organic synthesis, and wastewater treatment. The total output of H_2O_2 in China is statistically 12.39 million tons in 2021, which is chiefly produced through the traditional anthraquinone method. However, this synthetic method is energy-extensive, waste-generating, and expensive. While the direct electrolysis of H_2/O_2 over noble metal catalysts relies on the consumption of hydrogen [1–5]. Therefore, there is an urgent need to produce H_2O_2 in a cost-effective and eco-friendly manner.

Solar H_2O_2 production, driven by inexhaustible solar energy, merely relies on water, oxygen as well as a suitable photocatalyst, which gradually becomes a research hotspot [3,6–10]. In photocatalytic H_2O_2 production (PHP), the main challenges are the unsatisfactory charge separation efficiency and the detrimental backward decomposition of H_2O_2 . Targeting the first challenge, the usual practice is adding hole scavengers (such as isopropanol, ethanol, and ethylene glycol [11–15]),

aiming to suppress the recombination and enhance the utilization efficiency of electrons. Nevertheless, the transformation mechanism of added sacrificial agents is not very clear, resulting in the blind selection of sacrificial agents. Moreover, it is uneconomical since extra efforts are needed to separate H_2O_2 from the solvent-containing sacrificial agent [16]. Therefore, recently, H_2O_2 production from pure water has aroused much attention [10,17–19]. For instance, Zhang et al. [20] successfully introduced the $-C\equiv N$ groups (facilitate the adsorption of H^+) and N vacancies (adsorb and activate O_2) into $g-C_3N_4$ ($Nv-C\equiv N-CN$) sequentially, which not only enhances the light absorption and carrier separation, but also significantly improves the selectivity and activity of H_2O_2 generation from pure water. Han et al. [21] grafted (thio)urea functional groups onto covalent triazine frameworks (CTFs) and significantly-increased charge separation/transfer is achieved. Pitifully, the selected photocatalysts are limited to $g-C_3N_4$ -based and CTF-based composites, which suffer from intrinsically poor chemical and thermal stability. Moreover, the H_2O_2 production yield is still unsatisfactory to be put into industrial practice.

Besides, the poor performance is normally imputed to rapid electron-hole recombination since sacrificial agents are absent. To tackle the predicament, step-scheme (S-scheme) heterojunction becomes an

* Corresponding author.

E-mail address: zhangliuyang@cug.edu.cn (L. Zhang).

appealing choice, which has great potential in facilitating electron and hole separation and concurrently retaining strong oxidation and reduction abilities [22–25]. Herein, all-inorganic ZIS@BVO composites were designed, and demonstrated a PHP rate of $1.8 \text{ mmol g}^{-1} \text{ h}^{-1}$ in pure water, which is even comparable to its counterparts in the presence of scavengers, and co-catalysts. Combined with in-situ irradiated X-ray photoelectron spectroscopy (ISIXPS) results and density functional theory (DFT) calculation, the charge transfer mechanism is explicitly proposed.

It is generally acknowledged that the PHP process is composed of two major half-reactions [26–28]: one is the reduction of O_2 by photo-generated electrons; the other is the oxidation of H_2O by photogenerated holes. The role of singlet oxygens ($^1\text{O}_2$) in PHP has, however, received little attention, particularly among different inorganic materials. Unexpectedly, the characteristic peaks of $^1\text{O}_2$ have been observed in the all-inorganic ZIS@BVO composites. Previously, other reactions, such as the generation of radicals, are viewed as side reactions that are harmful in realizing high selectivity. Surprisingly, from the electron spin resonance spectroscopy (ESR) results and trapping results, the active species such as $\bullet\text{O}_2^-$, $^1\text{O}_2$, and $\bullet\text{OH}$ act as the bridge for the conversion of O_2 and H_2O , which do not inhibit H_2O_2 production, but instead they provide additional pathways for H_2O_2 production. Therefore, this study provides new insights into the mechanism of H_2O_2 production in the all-inorganic S-scheme heterojunction.

2. Experimental sections

2.1. Chemicals

All chemicals were in analytic purity and without further treatment. Zinc chloride (ZnCl_2), thioacetamide ($\text{C}_2\text{H}_5\text{NS}$, TAA), ethanol ($\text{C}_2\text{H}_5\text{OH}$), isopropanol ($\text{C}_3\text{H}_8\text{O}$, IPA), hydrochloric acid (HCl), N, N-dimethylformamide (DMF), and triethanolamine ($\text{C}_6\text{H}_{15}\text{NO}_3$) were purchased from Sinopharm Chemical Reagent Co., Ltd. While bismuth(III) nitrate pentahydrate ($\text{Bi}(\text{NO}_3)_3 \cdot 5 \text{ H}_2\text{O}$), indium chloride (InCl_3), manganese(III) acetate dihydrate ($\text{C}_6\text{H}_{13}\text{MnO}_8$), potassium iodide (KI), and p-Benzoquinone ($\text{C}_6\text{H}_4\text{O}_2$) were provided by Shanghai Macklin Biochemical Co., Ltd. Polyvinylpyrrolidone (PVP, 1,300,000), β -carotene, and vanadyl acetylacetone ($\text{C}_{10}\text{H}_{14}\text{O}_5\text{V}$) were purchased from Shanghai Aladdin Biochemical Technology Co., Ltd.

2.2. Preparation of BiVO_4 nanofibers

BiVO_4 nanofibers (BVO NFs) were prepared according to the reported electrospinning method with some modifications [29]. Specifically, 1.2 g of $\text{Bi}(\text{NO}_3)_3 \cdot 5 \text{ H}_2\text{O}$, 0.7 g of PVP, and 0.662 g of $\text{C}_{10}\text{H}_{14}\text{O}_5\text{V}$ were added into a mixture comprised of 2.0 g of CH_3COOH , 2.5 g of $\text{C}_2\text{H}_5\text{OH}$ and 2.5 g of DMF and stirred overnight. The homogeneous solution was injected into a 10 mL syringe. And the synthetic parameters were set as follows: electrode spacing was 15 cm; rotational speed was $35 \mu\text{L min}^{-1}$; voltage was 15 kV. Then, the spun nanofibers were dried at 80°C for 12 h and calcined at 500°C for 1.5 h in a furnace at 4°C min^{-1} .

2.3. Preparation of $\text{ZnIn}_2\text{S}_4\text{-BiVO}_4$ (ZB-X) composites and ZnIn_2S_4

The preparation procedure of ZB-X nanofibers is described as follows, where the suffix X represents the theoretical molar ratio of BVO NFs in $\text{ZnIn}_2\text{S}_4\text{/BiVO}_4$ composites. Typically, BVO (0.02 mmol) was dispersed in 20 mL of ultrapure water, and the pH was adjusted to be about 3, followed by the addition of certain amounts of ZnIn_2S_4 precursor (0.4 mmol ZnCl_2 and 0.8 mmol InCl_3 , 0.8 mmol of thioacetamide). Subsequently, the obtained mixture liquid was stirred for 30 min, whereafter it was put into an oil bath at 80°C and stirred constantly for 2 h. The obtained olivaceous products were centrifuged and washed repeatedly with deionized water and ethanol and dried for 10 h in a drying oven at 80°C . The as-obtained sample was denoted as

ZB-5, and ZB-10 and ZB-15 were prepared similarly. For comparison, the ZnIn_2S_4 nanosheets (NSs) were synthesized under the same conditions without the addition of BVO nanofibers.

3. Results and discussion

3.1. Structure and morphology

The crystal structures of the as-obtained catalysts were assessed by X-ray diffraction (XRD). The main characteristic peak at 28.9° of the BVO NFs (JCPDS No. 14–0688) was assigned to the (121) plane [30], as shown in Fig. 1a and b. Meanwhile, four characteristic peaks of the ZIS (JCPDS No. 65–2023) are located at 22.5° , 27.3° , 48.5° , and 57.5° , which belong to its (006), (102), (110), and (022) planes, respectively [31]. For the ZB-10 composite, because the peak intensity of BVO NFs is strong and the peak position overlaps with that of the ZIS, only two peaks at 27.3° and 48.5° can be assigned to ZIS. No characteristic peaks of other impurities were found, illustrating the successful synthesis of ZIS@BVO heterojunction.

The morphology of the as-prepared samples was evaluated via field emission scanning electron microscopy (FESEM). The electrospun BVO nanofibers have an average diameter of about 300–400 nm (Fig. 2a), and the bare ZIS nanosheets were randomly stacked (Fig. S1a, b). By contrast, the ZB-10, achieved by in-situ growth of ZIS on BVO, demonstrated a distinct core-shell structure with the BVO nanofibers as the backbone and ZIS nanosheets as the shell (Fig. 2b), which are intertwined to form a network. In the high-resolution transmission electron microscopy (HRTEM) images of the composite (Fig. S2), the lattice fringes of 0.293 nm can be attributed to the (104) plane of ZIS. Furthermore, the high-angle annular dark field (HAADF) image verifies the core-shell structure again. The ZIS nanosheets are almost diaphanous (Fig. 2c). And the elemental mapping (Fig. 2d) uncovers the spatial distribution of Bi, V, O, Zn, In, and S. Clearly, BVO fibers are in the interior, while the ZIS nanosheets are in the exterior, manifesting that the ZIS NSs are successfully grafted to the BVO NFs surface.

Brunauer–Emmett–Teller (BET) surface area and pore size distribution (Fig. S3) of the as-obtained samples were researched by N_2 physisorption at 77 K [32]. Both ZIS NSs and ZB-10 exhibit typical type-IV isotherms and a type-H₃ hysteresis loop, suggesting the existence of slit-shaped macropores. Whereas, no obvious hysteresis loop is detected in the BVO NFs sample. Moreover, ZIS NSs exhibit pores with diameters of approximately 2–100 nm, indicating the presence of mesopores and macropores, in agreement with the FESEM and TEM images (Fig. 2). Table S1 enumerates the BET surface area (S_{BET}), pore volume, and average pore diameter of the ZIS NSs, BVO NFs, and ZB-10. In contrast to pristine BVO NFs ($3.3 \text{ m}^2 \text{ g}^{-1}$), the S_{BET} of ZB-10 is increased by approximately 10 times after loading ZIS NSs.

3.2. Photoelectrochemical properties and charge transfer

The photocatalytic properties of the prepared catalysts are closely linked to the internal electronic structure and light absorption capacity. From their UV-Vis diffuse reflectance spectroscopy results (Fig. S4a), the absorption edges of the ZIS NSs and the BVO NFs stay at approximately 510 and 530 nm, respectively. Hence, both of them are responsive to visible light ($\lambda > 420 \text{ nm}$). With the increase in the BVO NFs content, the composite appears red-shift phenomenon, which coincides with the color change from bright yellow to earthy yellow. The band gaps and the positions of the conduction band (CB) and valence band (VB) of the BVO NFs and the ZIS NSs are examined. The band-gap energies (E_g) are calculated (Fig. S4b) to be 2.47 (BVO NFs) and 2.62 eV (ZIS NSs) respectively [24,33]. Judging from the M-S plots (Fig. S4c, d), both of these two components are classified to be n-type semiconductors. And the CB potentials of the BVO NFs and the ZIS NSs are estimated to be 0.05 and -0.81 V (vs. NHE), respectively. The calculated work functions of the BVO NFs and the ZIS NSs are 6.85 and 5.39 eV (Fig. S5a, b),

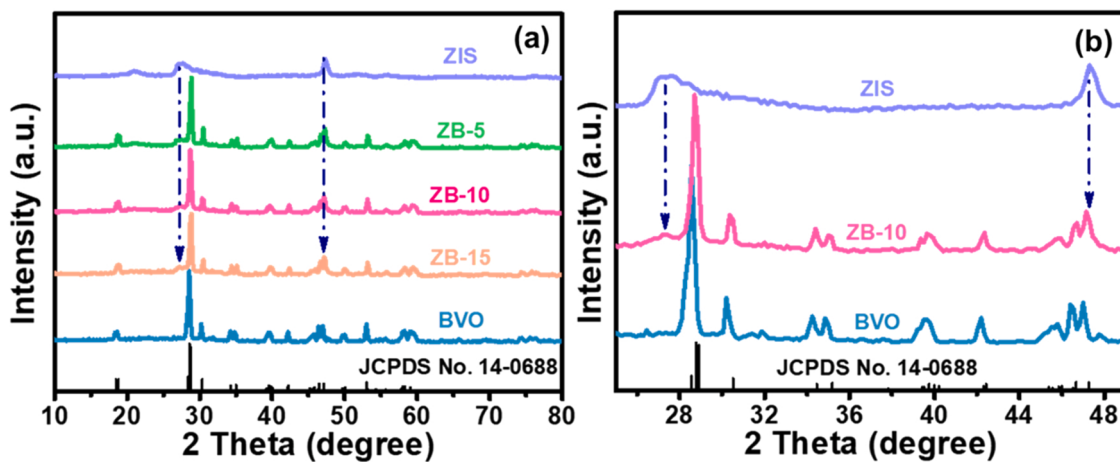


Fig. 1. (a, b) The XRD patterns of BVO, ZB-15, ZB-10, ZB-5, and ZIS.

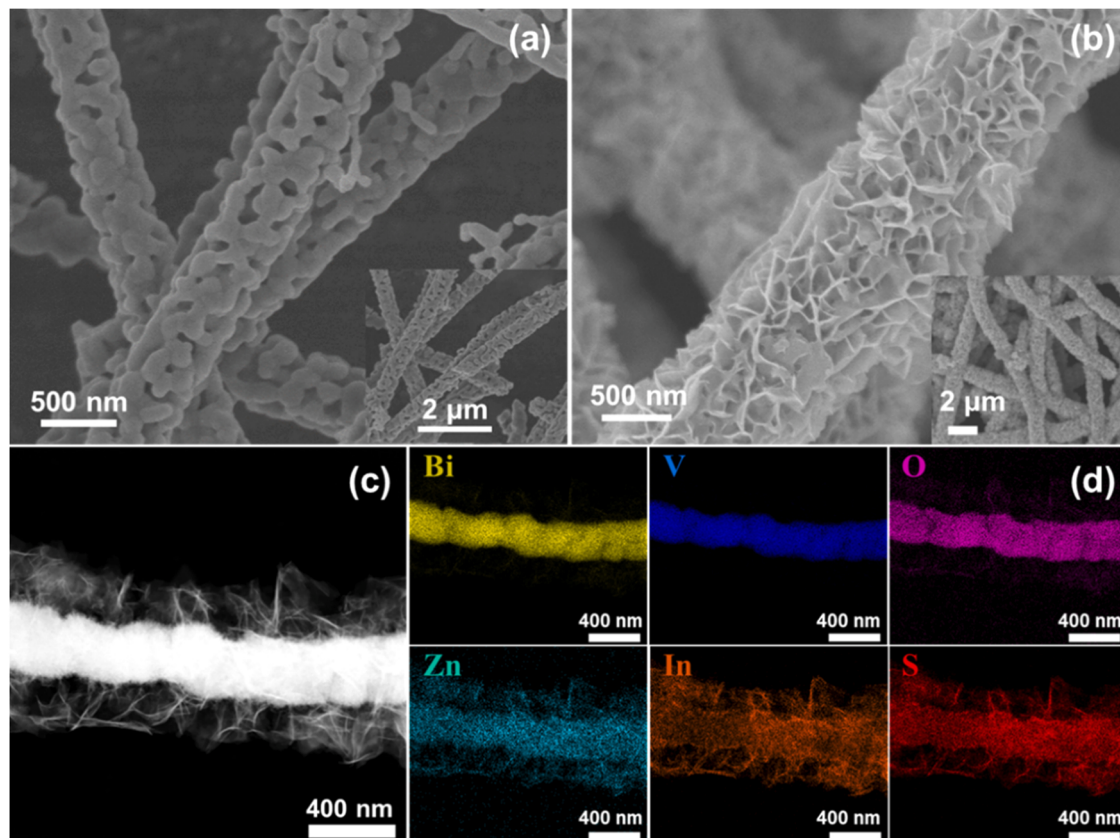


Fig. 2. SEM images of (a) BiVO₄, and (b) ZB-10 hybrids. (c)TEM images of ZB-10; (d) EDX mapping images of Bi, V, O, Zn, In, and S elements in ZB-10.

respectively. And the Fermi level of the BVO NFs is lower than that of ZIS NSs (Fig. S5c).

The electron transfer mechanism of ZIS, BVO, and ZB-10 composites was analyzed by ISIXPS [34,35,38]. The survey spectra (Fig. 3a) showed that the C, Zn, In, S (Bi, the peaks of the two elements are close to each other and cannot be distinguished), and O peaks in the ZB-10 [36,37]. Fig. 3b and c show the high-resolution XPS spectra of Zn 2p and In 3d of ZIS, and demonstrate a single oxidation state of Zn²⁺ (1022.16 eV, 1045.14 eV) and In³⁺ species (444.95 eV, 452.48 eV), respectively. In Fig. 3d, the peaks centered at 161.56 and 162.78 eV are attributed to the 2p_{3/2} and 2p_{1/2} of S, respectively. After the deposition of ZIS on the BVO surface, without irradiation, these peaks of ZIS shift to higher binding

energy by ~ 0.15 eV, indicating decreased electron density in ZIS. By contrast, the binding energy of Bi in BVO (Fig. 3d) migrates negatively by ~ 0.13 eV, manifesting increased electron density in BVO. The peak position changes for element O are hard to be detected due to their low surface contents (Fig. S6). Considering the Fermi level position as mentioned above, upon contact between the two semiconductors, the electrons transfer spontaneously from ZIS to BVO until equilibrium is reached. This coincides with the differential charge between the two contact surfaces (Figs. 3e and S5d): the charge density in ZIS NSs depletes whereas the charge density in BVO NFs accumulates. When ZB-10 is illuminated, the peaks of these elements move in opposite directions. Namely, electrons are transferred from BVO to ZIS, sacrificing these

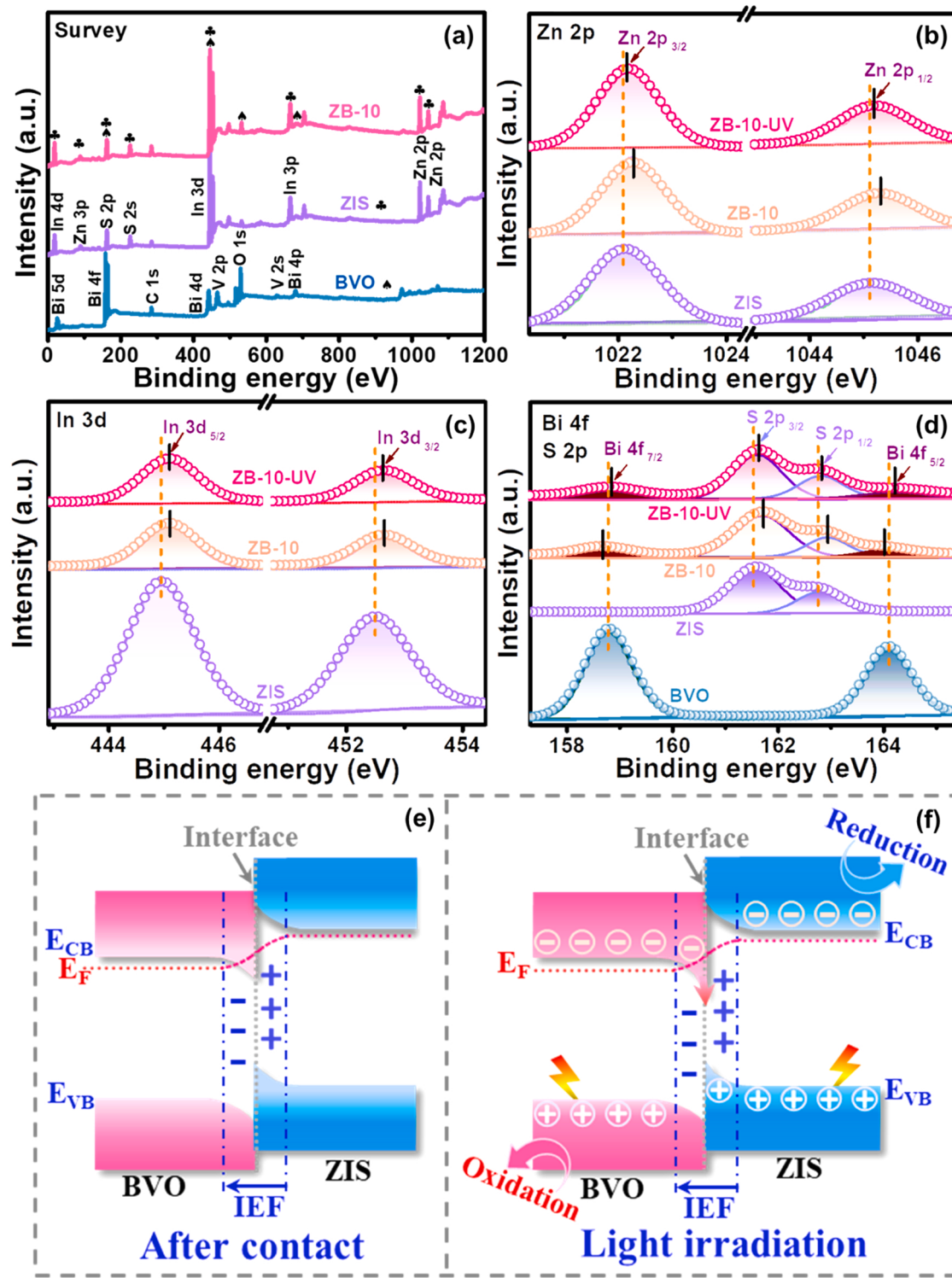


Fig. 3. ISIXPS spectra of (a) survey, (b) Zn 2p, (c) In 3d, and (d) Bi 4f and S 2p for BVO, ZIS, and ZB-10 under 365 nm LED irradiation. PHP mechanism of S-scheme heterojunction photocatalyst (e) after contact and (f) under light irradiation.

electrons and holes with low redox potential and maintaining those electrons and holes with strong redox potentials in the VB of BVO and the CB of ZIS (Fig. 3f). Consequently, the S-scheme charge transfer is corroborated.

3.3. Photocatalytic performance and carriers separate

To evaluate the PHP performance of the prepared samples, the

catalyst was placed in an O_2 -saturated solution, as shown in Fig. 4a. After irradiation by xenon lamp for one hour ($400 \text{ nm} \leq \lambda \leq 1000 \text{ nm}$), a negligible amount ($16 \mu\text{mol g}^{-1} \text{ h}^{-1}$) of H_2O_2 was detected in BVO NFs. The results disclose that the reduction ability of the BVO is insufficient to reduce O_2 to $\bullet O_2$, hence the yield of H_2O_2 is extremely low. While ZIS NSs show a relatively high H_2O_2 yield of $0.65 \text{ mmol g}^{-1} \text{ h}^{-1}$, which can be attributed to the large specific surface area and the appropriate band position. When the content of BVO NFs is 5%, the excessive ZIS will form

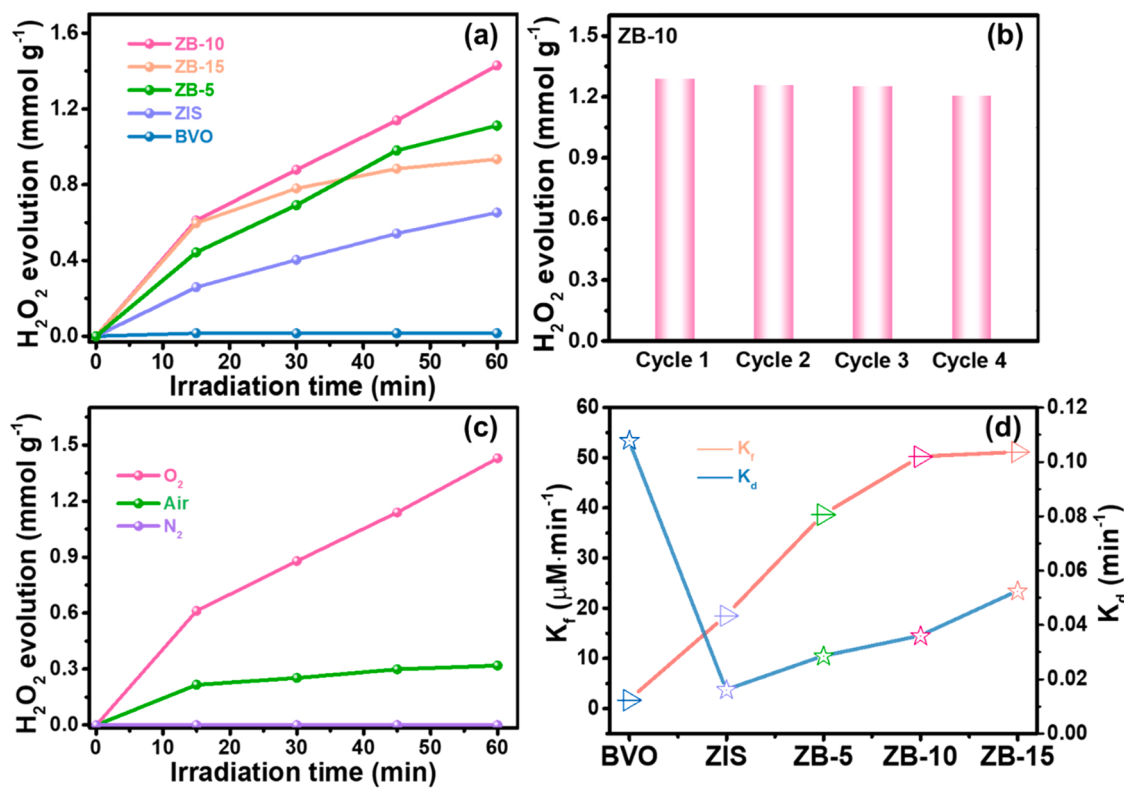


Fig. 4. (a) Production of H₂O₂ over as-prepared photocatalysts under visible light irradiation; (b) cycling durability for PHP on ZB-10; (c) effect of different atmospheres on PHP; (d) formation rate constant (K_f) and decomposition rate constant (K_d) for PHP.

self-aggregated particles (Fig. S7a), which will lead to the recombination of photogenerated carriers on the surface of the agglomerated ZIS. Distinctively, when the BVO content increases to 10%, the photocatalytic activity is significantly boosted, reaching about 1.4 mmol g⁻¹ after one hour of illumination, which is more than twice as much as that of bare ZIS NSs. However, when the proportion of BVO further increases to 15%, ZB-15 has fewer ZIS active sites than the other samples (Fig. S7b). Furthermore, the H₂O₂ evolution rates of ZB-10 and other photocatalysts decrease after fifteen minutes. This phenomenon may be related to the oxygen content in the liquid phase. Since the oxygen enters the closed system through bubbling, the oxygen content in the water is relatively high in the initial stage, which gradually decreases with the extension of illumination. Initially, oxygen diffusion cannot compensate for its consumption. Afterward, oxygen diffusion and consumption are dynamically balanced, which makes the production rate of H₂O₂ relatively stable. To verify the analysis, the photocatalytic performance of H₂O₂ in different oxygen concentrations was tested. As can be seen from Fig. S8a, the performance of H₂O₂ is gradually improved with the increase of oxygen content, which again proves that oxygen plays an important role in the process of H₂O₂ production. To demonstrate the repeatability of the composite samples, three batches of ZB-10 were synthesized and their performance was evaluated. It can be concluded from Fig. S8b that different batches of ZB-10 can still maintain the good photocatalytic performance of H₂O₂ production (up to 2.2 mmol g⁻¹ h⁻¹), which also indicates that the synthesis protocol has excellent performance repeatability. Subsequently, the cyclic stability of ZB-10 was tested (Fig. 4b) under identical conditions. The H₂O₂ yield declines mildly after four-cycle tests, which is attributed to catalyst loss during washing. The morphology and structure after photocatalysis are characterized by XRD and SEM. Fig. S9 shows the SEM images and the XRD patterns of ZB-10 before and after the photocatalytic reaction. Significantly, there are no noticeable morphological and structural alterations found for ZB-10, manifesting their photochemical robustness. In addition, the H₂O₂ production performance of ZB-10 under different

atmospheres was monitored (Fig. 4c). When N₂ is introduced, H₂O₂ cannot be detected, demonstrating that solar-driven water decomposition is difficult to achieve in pure water [20,39]. Whereas, the amount of hydrogen peroxide produced in the O₂-saturated atmosphere is about 4.5 times greater than that produced in air, again manifesting that oxygen molecules play an indispensable role in the whole reaction process. Notably, the formation and decomposition (i.e., H₂O₂ + e⁻ → •OH + OH⁻ [40,41]) of H₂O₂ coexist in the catalytic process. Therefore, the formation and decomposition rates of H₂O₂ on different catalysts were evaluated by fitting a quasi-first-order kinetic equation (Fig. 4d). In Eq. (1), the change of H₂O₂ concentration as a function of illumination time is speculated.

$$[\text{H}_2\text{O}_2] = \frac{K_f}{K_d}(1 - e^{-K_d t}) \quad (1)$$

where K_f (μM min⁻¹) and K_d (min⁻¹) are the formation and decomposition rate constant, respectively. From the fitting data, the K_f of ZIS NSs (16.9 μM min⁻¹) is much higher than that of BVO NFs (1.7 μM min⁻¹), uncovering that there are more active sites on the surface of the ZIS NSs, which are conducive to H₂O₂ production. As for the composite, with the increase in the BVO ratio from 5% to 15%, the K_f value increases markedly from 38.7 μM min⁻¹ (ZB-5) to 50.2 μM min⁻¹ (ZB-10) and then stabilizes at 51.2 μM min⁻¹ (ZB-15). The K_d value also rises with the increase in the loading of BVO (0.028–0.052). At the optimized ratio, ZB-10 has a high K_f value and the lowest K_d value, thus the formation of H₂O₂ can be greatly elevated and the decomposition of H₂O₂ can be suppressed.

The steady-state photoluminescence intensity (Fig. S10) of ZB-10 is lower than those of pristine ZIS and BVO, indicating that the establishment of an S-scheme heterojunction photocatalyst can tremendously restrain the recombination of photogenerated charge carriers. Moreover, the charge separation efficiency can be further researched by the photoelectrochemical technique. The TRPL spectra were also recorded

to gain a deeper insight into the charge transfer dynamics (Fig. 5a). The average PL lifetime (τ_{ave} , Table S2) of the ZB-10 (5.4 ns) is longer than those of pristine the ZIS NSs (2.7 ns) and the BVO NFs (2.5 ns). This also confirmed a more efficient separation and transfer of photogenerated carriers in the S-scheme heterojunction [42]. To further clarify the excellent performance of ZB-10, the separation and transfer dynamics of charge carriers were studied by the Fs-TAS. As shown in Fig. 5c and 5d, a broad positive absorption peak ranging from 630 to 770 nm appear for ZnIn_2S_4 , and ZB-10, which can be attributed to the typical excited-state absorption (ESA) of surface free or trapped photoexcited electrons in ZIS [43]. The decay curves at 716 nm and the corresponding three-exponential fitting results are shown in Fig. 5b. In comparison with ZIS ($\tau_{ave} = 1.25$ ns), the average lifetime of ZB-10 is extended 1.61 ns, suggesting that the S-scheme heterojunction can suppress the recombination rate of photogenerated electron-hole pairs, which is consistent with TRPL results.

Fig. S11a shows the periodic on/off transient photocurrent response of ZIS NSs, BVO NFs, and ZB-10. The pristine BVO NFs show a very low photocurrent density, which can be attributed to the fast recombination of photogenerated electrons and holes. By contrast, the ZB-10 composite shows higher anodic photocurrent intensity ($0.54 \mu\text{A cm}^{-2}$) than bare BVO ($0.08 \mu\text{A cm}^{-2}$) and ZIS ($0.36 \mu\text{A cm}^{-2}$), indicating that the hybrid composite holds a stronger ability in generating and transferring the photoexcited charge carrier under light irradiation. To further confirm the above results, electrochemical impedance spectroscopy (EIS, Fig. S11b) was performed. The Nyquist plot for the ZB-10 composite displays the smallest semicircle, specifying that the composite has a rock-bottom resistance among all the samples.

3.4. Photocatalytic mechanism

Furthermore, linear sweep voltammetry (LSV) tests were applied on a rotating disk electrode (RDE) [45]. Fig. S12a-c displays the LSV curves of ZIS NSs, BVO NFs, and ZB-10, respectively. The electric current density is incremental with the increasing rotating speed. The current density of the as-obtained samples consists of diffusion-controlled and reaction-kinetic-controlled parts. Fig. S12d displays the corresponding data fitted by the Koutecky-Levich (K-L) equation. The average number of electron transfers (n) over the O_2 reduction reaction was estimated by the slope. The n values of the ZB-10 and ZIS NSs are 1.75 and 2.3, indicating that the ZB-10 are more inclined to undergo a two-electron ORR process.

ESR technology can enable us to recognize the chief active species as well as study the mechanism of $^1\text{O}_2$ formation. As shown in Figs. 6a, 6c, and S13a, pronounced DMPO-• O_2^- and TEMP-• O_2 signal peaks are detected in ZB-10 and ZIS; while a fainter, split pattern is found in BVO (Fig. 6a), which is associated with the formation of DMPO-•OOH ($\text{O}_2/\bullet\text{OOH}$, $-0.05 \text{ V}_{\text{NHE}}$ [46]). These results manifest that a two-electron ORR process dominates in these samples, which is in accord with the LSV results. Furthermore, DMPO-•OH radicals only appear in ZB-10 and the BVO (in Fig. 6b). Although it is sometimes posited that the production of •OH is due to the decomposition of H_2O_2 , here, it is believed that •OH is generated through the reaction between photogenerated holes and adsorbed water molecules (or surface hydroxyl groups) because •OH is not found in ZIS. As for ZB-10, DMPO-•OH and DMPO-•OOH signals coexist, further proving the successful construction of S-scheme heterojunction. The $^1\text{O}_2$ signal of the modified ZB-10 catalyst is the strongest. This is attributed to the retained strong oxidation and reduction ability endowed by S-scheme heterojunction. In

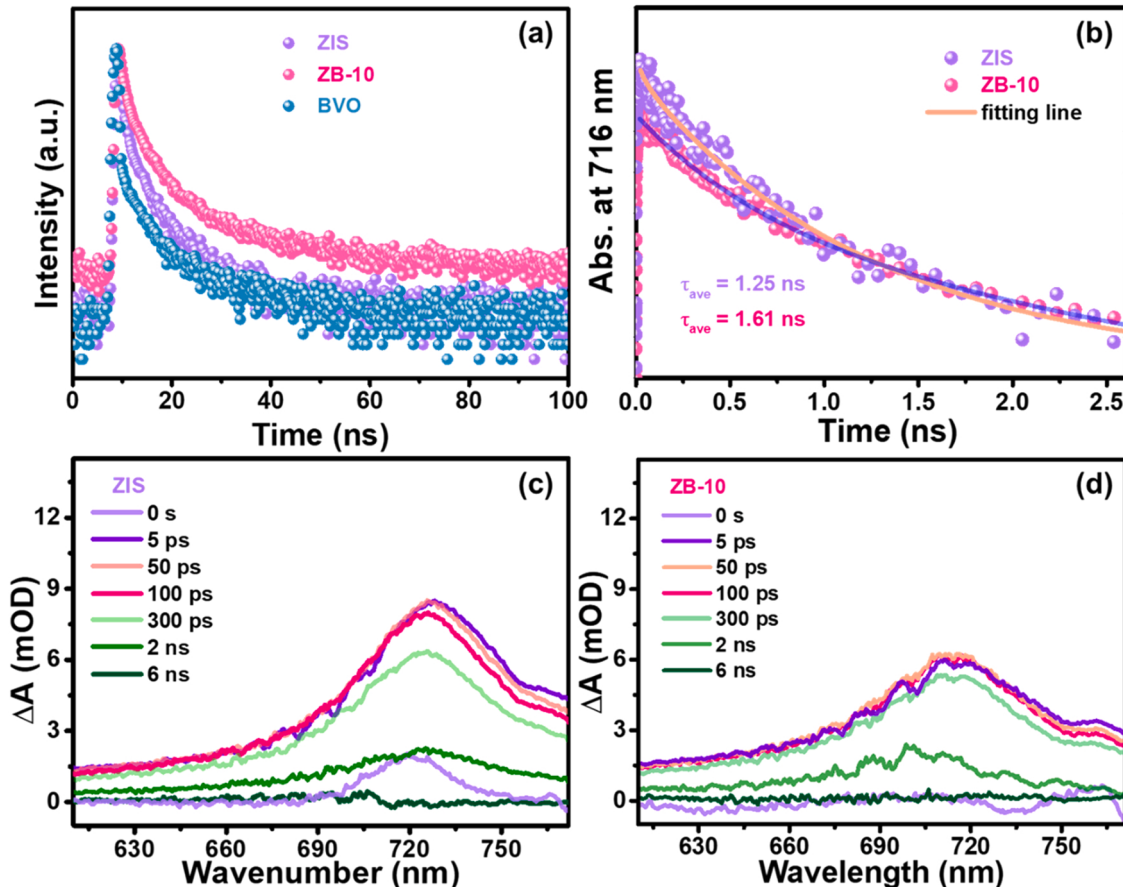


Fig. 5. (a) The time-resolved photoluminescence (TRPL) spectra; (b) the transient absorption kinetics probed at 716 nm. Femtosecond transient absorption spectra (Fs-TAS) of (c) ZIS and (d) ZB-10 in acetonitrile at different time delays under 400 nm laser excitation.

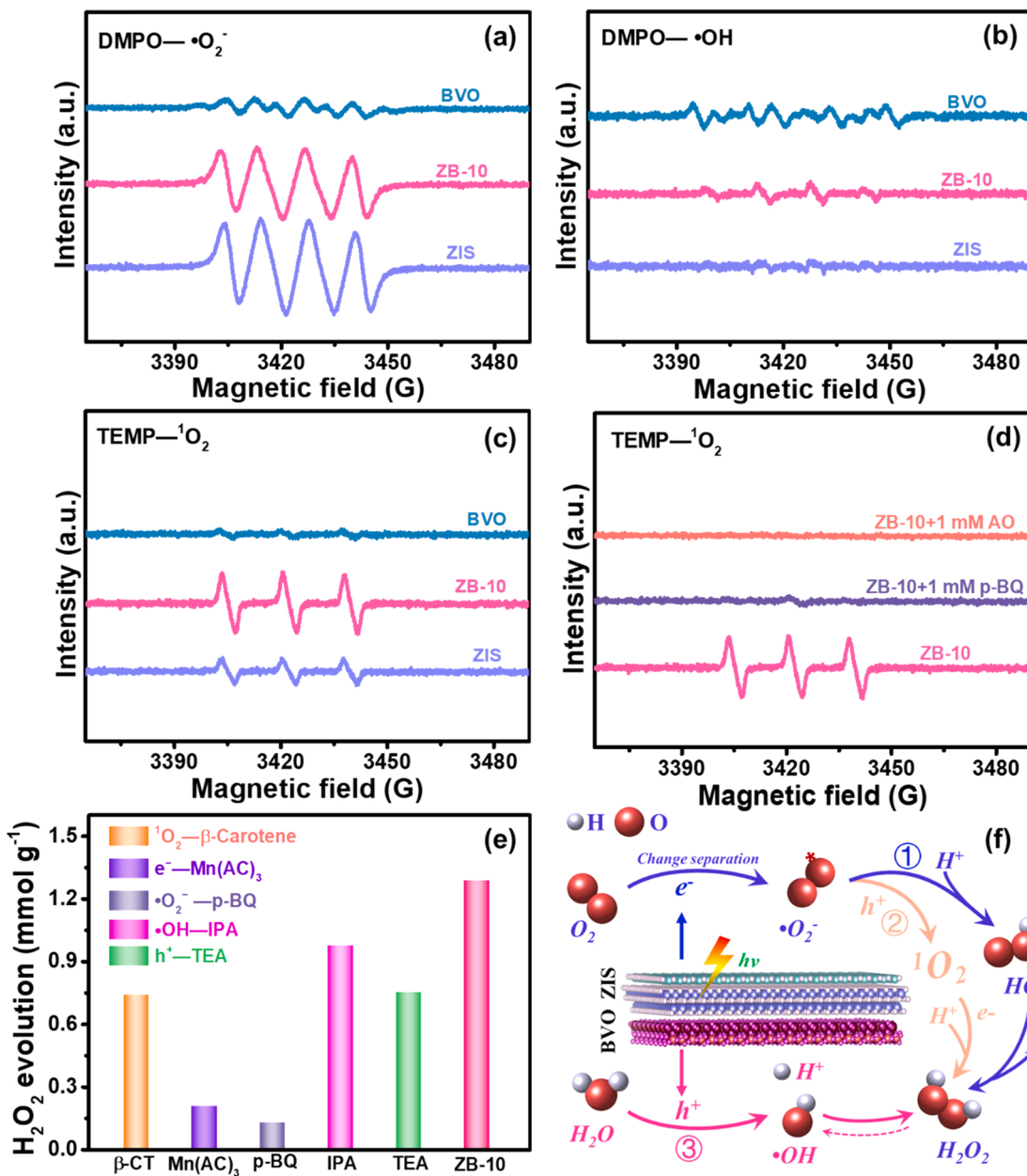


Fig. 6. DMPO spin-trapping ESR spectra for (a) $\bullet\text{O}_2^-$ in methanol and (b) $\bullet\text{OH}$ in water; TEMP spin-trapping experiments of the as-prepared samples for (c) $^1\text{O}_2$ in water; (d) ESR spectra for $^1\text{O}_2$ when adding $\bullet\text{O}_2^-$ trapping agent 1,4-benzoquinone (p-BQ, 1 mM) or adding h^+ trapping agent ammonium oxalate monohydrate (AO, 1 mM) of ZB-10; (e) Effects of a series of scavengers on the generation efficiency of H_2O_2 over ZB-10 (β -carotene, $\text{Mn}(\text{AC})_3\text{H}_2\text{O}$, p-BQ, isopropanol (IPA), and triethanolamine (TEOA) [44] (the number of scavengers 1 mM)); (f) the mechanism diagram of PHP over all-inorganic heterojunctions.

addition, to demonstrate the generation path of $^1\text{O}_2$ (0.34 V vs. NHE, $\bullet\text{O}_2^- + \text{h}^+ \rightarrow ^1\text{O}_2$) [47,48], ESR trapping experiments were conducted on ZB-10 and ZIS NSs, employing TEMP as a spin-trapping reagent, p-BQ as $\bullet\text{O}_2^-$ trapping agent and $(\text{NH}_4)_2\text{C}_2\text{O}_4$ as h^+ trapping agents (in Figs. 6d and S13b). After the addition of p-BQ, the ESR signal of $^1\text{O}_2$ cannot be detected over ZB-10 (the weak single peak is attributed to p-BQ), indicating that $^1\text{O}_2$ originates from $\bullet\text{O}_2^-$. Analogously, after the addition of $(\text{NH}_4)_2\text{C}_2\text{O}_4$, the $^1\text{O}_2$ signal drops steeply, illustrating that the h^+ also plays an indispensable role in the generation of $^1\text{O}_2$. Besides, no typical $^1\text{O}_2$ signal was found either in darkness or when O_2 was excluded, indicating that O_2 also plays a crucial role in the process of producing $^1\text{O}_2$ (Fig. S13c).

From the results of the trapping experiment of the ZB-10 (Fig. 6e) together with the aforementioned ESR results, it can be concluded that the chief active species for photocatalytic production of H_2O_2 are e^- and

$\bullet\text{O}_2^-$; while h^+ , $^1\text{O}_2$, and $\bullet\text{OH}$ also participate in the whole reaction [49, 50]. The reaction process is shown in the mechanism diagram (Fig. 6f). Particularly, after oxygen molecules are adsorbed on the surface of the catalyst, $\bullet\text{O}_2^-$ is generated via the reaction between O_2 and photo-generated electrons. Afterward, H_2O_2 can be produced from two paths from $\bullet\text{O}_2^-$. The principal path is its further reactions with electrons and H^+ . The secondary path is through the generation of $^1\text{O}_2$, which derives from the reaction between $\bullet\text{O}_2^-$ and accumulated holes. Subsequently, $^1\text{O}_2$ will further interact with e^- and H^+ to generate H_2O_2 . The latter represents an effective use of holes. Because holes are transferred rather than accumulating on the catalyst, which is beneficial to improve the separation of photogenerated carriers. When e^- or $\bullet\text{O}_2^-$ are captured, the performance of H_2O_2 is significantly reduced (down to about 10%), indicating that this pathway is the main pathway for H_2O_2 production. Also, the H_2O_2 can be tested, suggesting that two-electron WOR also

accounts for H_2O_2 generation using photogenerated holes. The two-electron WOR can be realized by a direct ($2 \text{H}_2\text{O} + 2 \text{h}^+ \rightarrow \text{H}_2\text{O}_2 + 2 \text{H}^+$, $E^0 = +1.76 \text{ V}$ vs. NHE) or an indirect process (1. $\text{H}_2\text{O} + \text{h}^+ \rightarrow \bullet\text{OH} + \text{H}^+$, $E^0 = +2.52 \text{ V}$ vs. NHE; 2. $\bullet\text{OH} + \bullet\text{OH} \rightarrow \text{H}_2\text{O}_2$). The direct process is more thermodynamically favorable (lower reaction potential), but is kinetically unfavorable (two photoinduced holes are needed to drive the reaction). By contrast, the indirect 2e^- WOR is kinetically favorable. Herein, $\bullet\text{OH}$ radicals are detected by ESR, indicating that the indirect process is dominant. Meanwhile, fluorescence spectroscopy is supplemented to evaluate the amount of produced $\bullet\text{OH}$, with coumarin and coumarin-3-carboxylic acid as the probes (coumarin and coumarin-3-carboxylic acid as the probes [51]). The amounts of $\bullet\text{OH}$ (both surface-adsorbed and free) produced by ZB-10 are much higher than the amounts of those produced by BVO (Fig. S15), implying a higher photocatalytic water oxidation capability for ZB-10. Moreover, the catalytic activity also decreases slightly when $\bullet\text{OH}$ is captured by IPA as well, and the influence of $\bullet\text{OH}$ on the production performance of H_2O_2 is proved again. When $^1\text{O}_2$ is captured, the catalytic activity dropped by 45%, indicating that $^1\text{O}_2$ plays an indispensable role in H_2O_2 production. When the h^+ was captured, the catalytic performance is also reduced by nearly half. It can be seen from the mechanism diagram that the h^+ mainly plays the role of oxidizing $\bullet\text{O}_2^-$ to generate $^1\text{O}_2$ or oxidizing H_2O to generate $\bullet\text{OH}$ in the reaction process. To illustrate the role of holes, when ethanol (10%) was added as a hole sacrificial agent (Fig. S14), the performance of H_2O_2 production decreased slightly. Therefore, in pure water, holes also participate in the generation of H_2O_2 as active species.

Besides, we also utilized in-situ infrared diffuse reflection spectrum (in-situ DRIFTS) measurements for real-time monitoring of the formation of H_2O_2 on the surfaces of different samples. When ZB-10 and ZIS were exposed to the mixture gases of H_2O (g) and O_2 , three leading peaks ($3684, 3580, 3213 \text{ cm}^{-1}$) were detected, and the intensity was gradually heightened with the extension of time in Fig. 7a and b, which

were attributed to the stretching vibrations of H_2O [52,53] and OH [54]. The intensity of these three peaks on the ZIS is stronger than that on ZB-10 during the adsorption stage, which may be attributed to the larger specific surface area of ZIS. The infrared spectra of ZB-10 and ZIS under visible light illumination were recorded when adsorption equilibrium was reached, as exhibited in Fig. 7c and d. The peak at 3415 cm^{-1} can be ascribed to the vibrational peak of HO-O^+ , which corresponds to the process of hydrogenation of $\bullet\text{O}_2^-$, again verifying that H_2O_2 is generated through a two-electron ORR process. Moreover, the newly emerged peak at 3237 cm^{-1} could be attributed to the representative O-H stretching in the formed H_2O_2 during the reaction process [55,56], and the peak is inch by inch increasing under light irradiation. The results directly validate that H_2O_2 was produced on ZB-10 and ZIS under photoirradiation.

4. Conclusion

This study pioneers the realization of solar on-site H_2O_2 generation over all-inorganic heterojunction without the assistance of sacrificial agents. The activity reaches up to about $1.8 \text{ mmol g}^{-1} \text{ h}^{-1}$ under visible light with fairly good stability, which even outperforms those utilizing sacrificial agents. The charge transfer in the heterojunction complies with the S-scheme heterojunction, as evidenced by the ISXPS, DFT calculation results, trapping experiments, and elongated lifetime from Fs-TAS. Attractively, a new interpretation of the pathways to H_2O_2 generation in pure water is provided. Especially, the intermediate transformation from $\bullet\text{O}_2^-$ to $^1\text{O}_2$ and finally to H_2O_2 is proved to contribute to the H_2O_2 formation. This finding supplies the formation pathway and the development of this system will offer guidance on the design of stable photocatalysts for efficient in-situ production of H_2O_2 in pure water in the future.

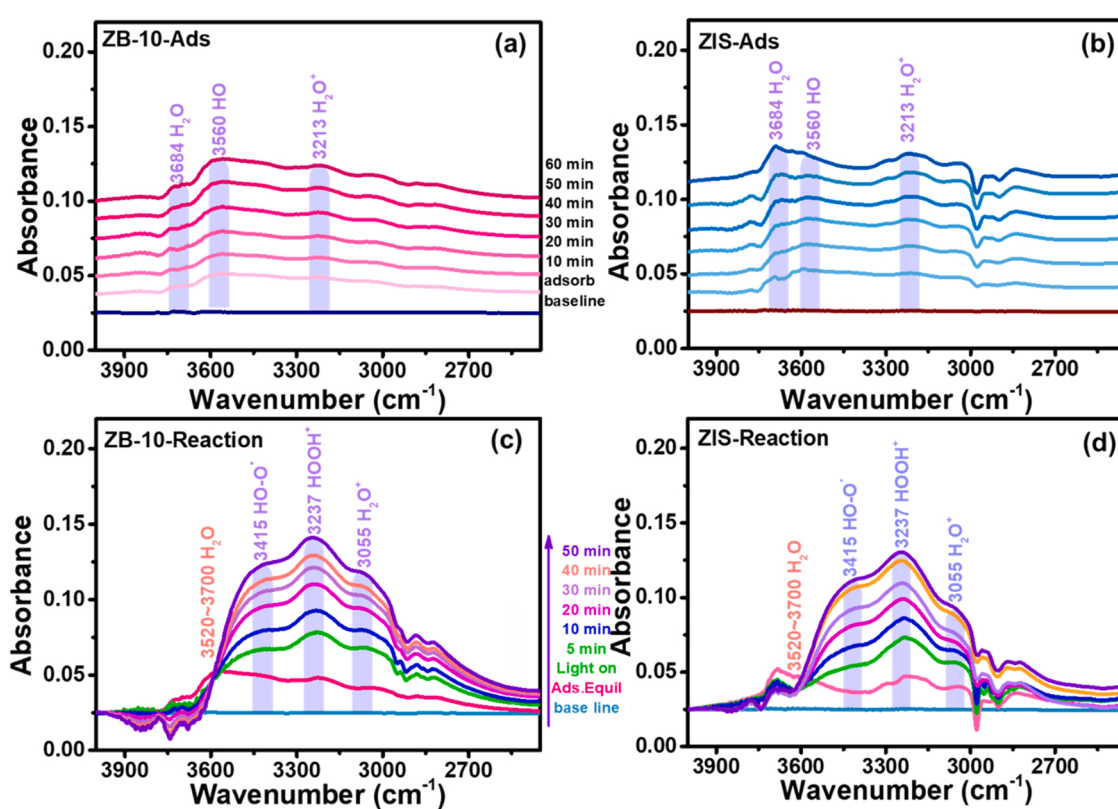


Fig. 7. In-situ DRIFTS spectra obtained on (a) ZB-10 and (b) ZIS NSs adsorb H_2O and O_2 under the dark state, and (c) ZB-10 and (d) ZIS NSs under light irradiation ($\lambda = 420 \text{ nm}$).

CRediT authorship contribution statement

Miaoli Gu: Investigation, Methodology, Data curation, Formal analysis, Visualization, Writing – original draft. **Yi Yang:** Methodology, Visualization, Formal analysis. **Liuyang Zhang:** Data curation, Conceptualization, Visualization, Writing – review & editing. **Bicheng Zhu:** DFT calculations, Data curation. **Guojie Liang:** Resources, Supervision. **Jaoguo Yu:** Supervision, Conceptualization, Writing – review & editing.

Declaration of Competing Interest

The authors declare that they have no known competing financial interests or personal relationships that could have appeared to influence the work reported in this paper.

Data availability

Data will be made available on request.

Acknowledgments

This work was supported by the National Natural Science Foundation of China (NSFC) (Nos. 51872220, 22278383, 51932007, 52173065, 52073223 and U1905215).

Appendix A. Supplementary material

Supplementary data associated with this article can be found in the online version at [doi:10.1016/j.apcatb.2022.122227](https://doi.org/10.1016/j.apcatb.2022.122227).

References

- [1] K.H. Kim, S.J. Kim, W.H. Choi, H. Lee, B.C. Moon, G.H. Kim, J.W. Choi, D.G. Park, J.H. Choi, H. Kim, J.K. Kang, Triphasic metal oxide photocatalyst for reaction site-specific production of hydrogen peroxide from oxygen reduction and water oxidation, *Adv. Energy Mater.* 12 (2022) 2104052.
- [2] H. Li, P. Wen, D.S. Itanze, Z.D. Hood, S. Adhikari, C. Lu, X. Ma, C. Dun, L. Jiang, D. L. Carroll, Y. Qiu, S.M. Geyer, Scalable neutral H₂O₂ electrosynthesis by platinum diphosphide nanocrystals by regulating oxygen reduction reaction pathways, *Nat. Commun.* 11 (2020) 3928.
- [3] H. Hou, X. Zeng, X. Zhang, Production of hydrogen peroxide by photocatalytic processes, *Angew. Chem. Int. Ed.* 59 (2020) 17356–17376.
- [4] X. Zeng, Y. Liu, X. Hu, X. Zhang, Photoredox catalysis over semiconductors for light-driven hydrogen peroxide production, *Green Chem.* 23 (2021) 1466–1494.
- [5] K. Jiang, J. Zhao, H. Wang, Catalyst design for electrochemical oxygen reduction toward hydrogen peroxide, *Adv. Funct. Mater.* 30 (2020) 2003321.
- [6] C. Pan, G. Bian, Y. Zhang, Y. Lou, Y. Zhang, Y. Dong, J. Xu, Y. Zhu, Efficient and stable H₂O₂ production from H₂O and O₂ on BiPO₄ photocatalyst, *Appl. Catal. B Environ.* 316 (2022), 121675.
- [7] Z. Teng, Q. Zhang, H. Yang, K. Kato, W. Yang, Y.R. Lu, S. Liu, C. Wang, A. Yamakata, C. Su, B. Liu, T. Ohno, Atomically dispersed antimony on carbon nitride for the artificial photosynthesis of hydrogen peroxide, *Nat. Catal.* 4 (2021) 374–384.
- [8] L. Liu, M.Y. Gao, H. Yang, X. Wang, X. Li, A.I. Cooper, Linear conjugated polymers for solar-driven hydrogen peroxide production: the importance of catalyst stability, *J. Am. Chem. Soc.* 143 (2021) 19287–19293.
- [9] C. Chu, Q. Li, W. Miao, H. Qin, X. Liu, D. Yao, S. Mao, Photocatalytic H₂O₂ production driven by cyclodextrin-pyrimidine polymer in a wide pH range without electron donor or oxygen aeration, *Appl. Catal. B Environ.* 314 (2022), 121485.
- [10] T. Liu, Z. Pan, J.J.M. Vequizo, K. Kato, B. Wu, A. Yamakata, K. Katayama, B. Chen, C. Chu, K. Domen, Overall photosynthesis of H₂O₂ by an inorganic semiconductor, *Nat. Commun.* 13 (2022) 1034.
- [11] B. Liu, C. Bie, Y. Zhang, L. Wang, Y. Li, J. Yu, Hierarchically porous ZnO/g-C₃N₄ S-scheme heterojunction photocatalyst for efficient H₂O₂ production, *Langmuir* 37 (2021) 14114–14124.
- [12] L. Wang, B. Li, D.D. Dionysiou, B. Chen, J. Yang, J. Li, Overlooked formation of H₂O₂ during the hydroxyl radical-scavenging process when using alcohols as scavengers, *Environ. Sci. Technol.* 56 (2022) 3386–3396.
- [13] L. Xu, Y. Liu, L. Li, Z. Hu, J.C. Yu, Fabrication of a photocatalyst with biomass waste for H₂O₂ synthesis, *ACS Catal.* 11 (2021) 14480–14488.
- [14] Y. Zhang, J. Qiu, B. Zhu, M.V. Fedin, B. Cheng, J. Yu, L. Zhang, ZnO/COF S-scheme heterojunction for improved photocatalytic H₂O₂ production performance, *Chem. Eng. J.* 444 (2022), 136584.
- [15] Z. Jiang, Y. Zhang, L. Zhang, B. Cheng, L. Wang, Effect of calcination temperatures on photocatalytic H₂O₂-production activity of ZnO nanorods, *Chin. J. Catal.* 43 (2022) 226–233.
- [16] J. Liu, Y. Zou, B. Jin, K. Zhang, J.H. Park, Hydrogen peroxide production from solar water oxidation, *ACS Energy Lett.* 4 (2019) 3018–3027.
- [17] X. Chen, W. Zhang, L. Zhang, L. Feng, C. Zhang, J. Jiang, H. Wang, Construction of porous tubular In₂S₃@In₂O₃ with plasma treatment-derived oxygen vacancies for efficient photocatalytic H₂O₂ production in pure water via two-electron reduction, *ACS Appl. Mater. Interfaces* 13 (2021) 25868–25878.
- [18] H. Hirakawa, S. Shiota, Y. Shiraishi, H. Sakamoto, S. Ichikawa, T. Hirai, Au nanoparticles supported on BiVO₄: effective inorganic photocatalysts for H₂O₂ production from water and O₂ under visible light, *ACS Catal.* 6 (2016) 4976–4982.
- [19] L. Chen, L. Wang, Y. Wan, Y. Zhang, Z. Qi, X. Wu, H. Xu, Acetylene and diacetylene functionalized covalent triazine frameworks as metal-free photocatalysts for hydrogen peroxide production: a new two-electron water oxidation pathway, *Adv. Mater.* 32 (2020) 1904433.
- [20] X. Zhang, P. Ma, C. Wang, L. Gan, X. Chen, P. Zhang, Y. Wang, H. Li, L. Wang, X. Zhou, K. Zheng, Unraveling the dual defect sites in graphite carbon nitride for ultra-high photocatalytic H₂O₂ evolution, *Energy Environ. Sci.* 15 (2022) 830–842.
- [21] C. Wu, Z. Teng, C. Yang, F. Chen, H.B. Yang, L. Wang, H. Xu, B. Liu, G. Zheng, Q. Han, Polarization engineering of covalent triazine frameworks for highly efficient photosynthesis of hydrogen peroxide from molecular oxygen and water, *Adv. Mater.* 34 (2022) 2110266.
- [22] L. Zhang, J. Zhang, H. Yu, J. Yu, Emerging S-scheme photocatalyst, *Adv. Mater.* 34 (2022) 2107668.
- [23] L. Wang, J. Zhang, Y. Zhang, H. Yu, Y. Qu, J. Yu, Inorganic metal-oxide photocatalyst for H₂O₂ production, *Small* 18 (2022) 2104561.
- [24] L. Li, D. Ma, Q. Xu, S. Huang, Constructing hierarchical ZnIn₂S₄/g-C₃N₄ S-scheme heterojunction for boosted CO₂ photoreduction performance, *Chem. Eng. J.* 437 (2022), 135153.
- [25] R. He, D. Xu, X. Li, Floatable S-scheme photocatalyst for H₂O₂ production and organic synthesis, *J. Mater. Sci. Technol.* 138 (2023) 256–258.
- [26] X. Chen, Y. Kondo, S. Li, Y. Kuwahara, K. Mori, D. Zhang, C. Louis, H. Yamashita, Visible-light-driven hydrogen peroxide production from water and dioxygen by perylenetetracarboxylic diimide modified titanium-based metal-organic frameworks, *J. Mater. Chem. A* 9 (2021) 26371–26380.
- [27] Y. Yang, B. Zhu, L. Wang, B. Cheng, L. Zhang, J. Yu, In-situ grown N, S co-doped graphene on TiO₂ fiber for artificial photosynthesis of H₂O₂ and mechanism study, *Appl. Catal. B Environ.* 317 (2022), 121788.
- [28] L. Wang, J. Zhang, H. Yu, I.H. Patir, Y. Li, S. Wageh, A.A. Al-Ghamdi, J. Yu, Dynamics of photogenerated charge carriers in inorganic/organic s-scheme heterojunctions, *J. Phys. Chem. Lett.* 13 (2022) 4695–4700.
- [29] L.G. Peng, H. Wang, J. Liu, M. Sun, F.R. Ni, M.J. Chang, H.L. Du, J. Yang, Fabrication of fibrous BiVO₄/Bi₂S₃/MoS₂ heterojunction and synergistic enhancement of photocatalytic activity towards pollutant degradation, *J. Solid State Chem.* 299 (2021), 122195.
- [30] D. Gogoi, A.K. Shah, P. Rambabu, M. Qureshi, A.K. Golder, N.R. Peela, Step-scheme heterojunction between CdS nanowires and facet-selective assembly of MnO_x-BiVO₄ for an efficient visible-light-driven overall water splitting, *ACS Appl. Mater. Interfaces* 13 (2021) 45475–45487.
- [31] Y. Xia, Q. Li, K.L. Lv, D. Tang, M. Li, Superiority of graphene over carbon analogs for enhanced photocatalytic H₂-production activity of ZnIn₂S₄, *Appl. Catal. B Environ.* 206 (2017) 344–352.
- [32] H. Liu, J. Zhang, D. Ao, Construction of heterostructured ZnIn₂S₄@NH₂-MIL-125 (Ti) nanocomposites for visible-light-driven H₂ production, *Appl. Catal. B Environ.* 221 (2018) 433–442.
- [33] W. Zhao, Y. Feng, J. Zhang, F. Zhu, Z. Sheng, B. Dai, D.Y.C. Leung, L. Zhang, J. Xu, Novel Ag/p-AgBr/n-BiVO₄ plasmonic heterojunction photocatalyst: study on the excellent photocatalytic performance and photocatalytic mechanism, *ACS Appl. Energy Mater.* 2 (2019) 694–704.
- [34] Z. Jiang, B. Cheng, Y. Zhang, S. Wageh, A.A. Al-Ghamdi, J. Yu, L. Wang, S-scheme ZnO/WO₃ heterojunction photocatalyst for efficient H₂O₂ production, *J. Mater. Sci. Technol.* 124 (2022) 193–201.
- [35] B. He, Z. Wang, P. Xiao, T. Chen, J. Yu, L. Zhang, Cooperative coupling of H₂O₂ production and organic synthesis over a floatable polystyrene-sphere-supported TiO₂/Bi₂O₃ S-scheme photocatalyst, *Adv. Mater.* 34 (2022) 2203225.
- [36] Y. Xia, B. Cheng, J. Fan, J. Yu, G. Liu, Near-infrared absorbing 2D/3D ZnIn₂S₄/N-doped graphene photocatalyst for highly efficient CO₂ capture and photocatalytic reduction, *Sci. China Mater.* 63 (2020) 552–565.
- [37] J. Hu, C. Chen, Y. Zheng, G. Zhang, C. Guo, C.M. Li, Spatially separating redox centers on Z-scheme ZnIn₂S₄/BiVO₄ hierarchical heterostructure for highly efficient photocatalytic hydrogen evolution, *Small* 16 (2020), e2002988.
- [38] J. Zhang, L. Zhang, W. Wang, J. Yu, In situ irradiated X-ray photoelectron spectroscopy investigation on electron transfer mechanism in S-scheme photocatalyst, *J. Phys. Chem. Lett.* 13 (2022) 8462–8469.
- [39] C. Bie, L. Wang, J. Yu, Challenges for photocatalytic overall water splitting, *Chem* 8 (2022) 1567–1574.
- [40] H. Tian, Y. Wang, Y. Pei, Energy capture from thermolytic solutions and simulated sunlight coupled with hydrogen peroxide production and wastewater remediation, *Water Res.* 170 (2020), 115318.
- [41] J. Luo, Y. Liu, C. Fan, L. Tang, S. Yang, M. Liu, M. Wang, C. Feng, X. Ouyang, L. Wang, L. Xu, J. Wang, M. Yan, Direct attack and indirect transfer mechanisms dominated by reactive oxygen species for photocatalytic H₂O₂ production on g-C₃N₄ possessing nitrogen vacancies, *ACS Catal.* 11 (2021) 11440–11450.

[42] G. Han, F. Xu, B. Cheng, Y. Li, J. Yu, L. Zhang, Enhanced photocatalytic H_2O_2 production over inverse opal $ZnO@polydopamine$ S-scheme heterojunctions, *Acta Phys. Chim. Sin.* 38 (2022) 2112037.

[43] X. Shi, L. Mao, C. Dai, P. Yang, J. Zhang, F. Dong, L. Zheng, M. Fujitsuka, H. Zheng, Inert basal plane activation of two-dimensional $ZnIn_2S_4$ via Ni atom doping for enhanced co-catalyst free photocatalytic hydrogen evolution, *J. Mater. Chem. A* 8 (2020) 13376–13384.

[44] X. Geng, L. Wang, L. Zhang, H. Wang, Y. Peng, Z. Bian, H_2O_2 production and in situ sterilization over a $ZnO/g-C_3N_4$ heterojunction photocatalyst, *Chem. Eng. J.* 420 (2021), 129722.

[45] Y. Shao, J. Hu, T. Yang, X. Yang, J. Qu, Q. Xu, C.M. Li, Significantly enhanced photocatalytic in-situ H_2O_2 production and consumption activities for efficient sterilization by $ZnIn_2S_4/g-C_3N_4$ heterojunction, *Carbon* 190 (2022) 337–347.

[46] S.A. Bonke, T. Rissee, A. Schnegg, A. Brückner, In situ electron paramagnetic resonance spectroscopy for catalysis, *Nat. Rev. Methods Prim.* 1 (2021) 33.

[47] S. Zhao, X. Zhao, Insights into the role of singlet oxygen in the photocatalytic hydrogen peroxide production over polyoxometalates-derived metal oxides incorporated into graphitic carbon nitride framework, *Appl. Catal. B Environ.* 250 (2019) 408–418.

[48] J. Luo, C. Fan, L. Tang, Y. Liu, Z. Gong, T. Wu, X. Zhen, C. Feng, H. Feng, L. Wang, L. Xu, M. Yan, Reveal Bronsted–Evans–Polanyi relation and attack mechanisms of reactive oxygen species for photocatalytic H_2O_2 production, *Appl. Catal. B Environ.* (2022), 120757.

[49] Y. Nosaka, A.Y. Nosaka, Generation and detection of reactive oxygen species in photocatalysis, *Chem. Rev.* 117 (2017) 11302–11336.

[50] X. Xu, J. Wang, T. Chen, N. Yang, S. Wang, X. Ding, H. Chen, Deep insight into ROS mediated direct and hydroxylated dichlorination process for efficient photocatalytic sodium pentachlorophenate mineralization, *Appl. Catal. B Environ.* 296 (2021), 120352.

[51] X. Cao, A. Huang, C. Liang, H.C. Chen, T. Han, R. Lin, Q. Peng, Z. Zhuang, R. Shen, H.M. Chen, Y. Yu, C. Chen, Y. Li, Engineering lattice disorder on a photocatalyst: photochromic biobr nanosheets enhance activation of aromatic C–H bonds via water oxidation, *J. Am. Chem. Soc.* 144 (2022) 3386–3397.

[52] L.I. Yeh, M. Okumura, J.D. Myers, J.M. Price, Y.T. Lee, Vibrational spectroscopy of the hydrated hydronium cluster ions $H_3O^+ \cdot (H_2O)_n$ ($n=1, 2, 3$), *J. Chem. Phys.* 91 (1989) 7319–7330.

[53] T.R. Huet, C.J. Pursell, W.C. Ho, B.M. Dinelli, T. Oka, Infrared spectroscopy and equilibrium structure of $H_2O+(X^2 B_1)$, *J. Chem. Phys.* 97 (1992) 5977–5987.

[54] M. Okumura, L.I. Yeh, J.D. Myers, Y.T. Lee, Infrared spectra of the solvated hydronium ion: vibrational predissociation spectroscopy of mass-selected $H_3O^+ (H_2O)_n^* (H_2)_{lm}$, *J. Phys. Chem.* 94 (1990) 3416–3427.

[55] H. Cheng, H. Lv, J. Cheng, L. Wang, X. Wu, H. Xu, Rational design of covalent heptazine frameworks with spatially separated redox centers for high-efficiency photocatalytic hydrogen peroxide production, *Adv. Mater.* 34 (2022) 2107480.

[56] M. Kou, Y. Wang, Y. Xu, L. Ye, Y. Huang, B. Jia, H. Li, J. Ren, Y. Deng, J. Chen, Y. Zhou, K. Lei, L. Wang, W. Liu, H. Huang, T. Ma, Molecularly engineered covalent organic frameworks for hydrogen peroxide photosynthesis, *Angew. Chem. Int. Ed.* 61 (2022) 202200413.